LOCAL TOMOGRAPHY IN ELECTRON MICROSCOPY*

ERIC TODD QUINTO† AND OZAN ÖKTEM‡

Abstract. We present a new local tomographic algorithm applicable to electron microscope tomography. Our algorithm applies to the standard data acquisition method, single-axis tilting, as well as to more arbitrary acquisition methods including double axis and conical tilt. Using microlocal analysis we put the reconstructions in a mathematical context, explaining which singularities are stably visible from the limited data given by the data collection protocol in the electron microscope. Finally, we provide reconstructions of real specimens from electron tomography data.

Key words. X-ray transform, limited data tomography, microlocal analysis, Lambda tomography, electron tomography

AMS subject classifications. Primary, 44A12, 92C55; Secondary, 65R30, 35S30

DOI. 10.1137/07068326X

1. Introduction. Our goal is to show how singularity detection algorithms can be useful in *electron (microscope) tomography (ET)*. Briefly, given *transmission electron microscope (TEM)* data and using principles of tomography, the goal in ET is to reconstruct the scattering potential of the individual molecules in an in situ (in the cellular environment) or in vitro (in aqueous environment) specimen, each of which can be fairly arbitrary. Because the specimen extends far beyond the area exposed to the electrons, the exposed region covers only a small subregion, which is usually referred to as the *region of interest*. Again, because of the size of the whole specimen, one can rotate it only in a limited range of angles, so the reconstruction problem is a *limited angle* problem. These imply that one has *nonuniqueness* and *severe ill-posedness*. Nonuniqueness, as illustrated in Example 3.1, means that one cannot exactly reconstruct the scattering potential of the specimen even in cases when one assumes exact data (no measurement errors) and disregards the discretization of the set of lines (i.e., one deals with the corresponding continuous problem where data are given over a continuous set of lines). Furthermore, as discussed in section 2.2, the data are very noisy, in particular because of the dose problem—the dose needed to get low-noise data destroys the specimen. Since the limited angle problem leads to severe ill-posedness, the reconstruction problem is unstable and the noise in the data is amplified.

These issues, namely nonuniqueness and ill-posedness, point to using a reconstruction method that regularizes by reconstructing only some information about the specimen that can be stably retrieved, in our case the shape of the boundaries of the molecules in the specimen. Our method is a generalization of Lambda tomography [6, 28].

The article is organized as follows. In section 2, we give the background from physics and state the inverse problem. To provide perspective, we briefly describe

planar Lambda tomography in section 3. Next, we provide our general algorithm for arbitrary data sets in section 4. Then, in section 5 we give the specifics for single-axis tilt ET. In section 6, we describe which singularities of the specimen are stably recoverable from the limited data in ET. We put our results in the context of microlocal analysis as done by [20] for planar CT. This is based on the theory of Fourier integral operators, and the specific results are based on very general theorems in [8] or [2]. Finally, in section 7, we give reconstructions from real data to illustrate the efficiency of our algorithm and demonstrate our characterization of stably recoverable singularities. The appendix includes proofs of our technical theorems.

2. Electron (microscope) tomography (ET). In what follows we will provide a very brief overview of ET, where our aim is to properly state the inverse problem and show how integral geometry can be used to solve it. The reader is referred to [4] and the references therein for a more detailed account.

2.1. Scientific application and experimental setting. The problem of recovering the three-dimensional structure of an individual molecule (e.g., a protein or a macromolecular assembly) at the highest possible resolution in situ or in vitro plays a central role in understanding biological processes in time and space. Established approaches, such as X-ray crystallography and nuclear magnetic resonance (NMR), for dealing with this problem cannot recover the structure of an *individual* molecule in a sample. The publication of [3, 29, 11] in 1968 marked the beginning of ET, where the idea of recovering the structure of a sample from TEM data using principles of tomography was first outlined. ET is currently the *only* approach that allows one to reconstruct the three-dimensional structure of *individual* molecules in in situ/in vitro samples. The main drawback of ET when compared to NMR/X-ray crystallography, mentioned earlier, is that it provides only a low-resolution structure due to reasons explained in section 2.2. However, since the ability to study individual molecules is important in order to address many biological problems, ET is nowadays enjoying an increasing interest within life sciences as a technique for low- or medium-resolution structure determination of individual molecules.

A specimen that is to be imaged in a TEM must first be physically immobilized since it is imaged in a vacuum. It also needs to be thin (about 70–100 nm) if enough electrons are to pass through to form an image. The purpose of sample preparation is to achieve this *without interfering with the structure of the specimen*. Data collection in ET is done by mounting the specimen on a holder (goniometer) that allows one to change its positioning relative to the optical axis of the TEM. For a fixed position, the specimen is radiated with an electron beam, and the resulting data, referred to as a *micrograph*, is recorded by a detector. Hence, each fixed orientation of the specimen yields one micrograph, and the procedure is then repeated for a set of different positions. The most common data acquisition geometry is *single-axis tilting*, where the specimen plane is allowed only to rotate around a fixed single axis, called the *tilt axis*, which is orthogonal to the optical axis of the TEM. The rotation angle is called the *tilt angle*, and its angular range is usually contained in a subset of $[-60°, 60°]$.

2.2. Difficulties. Limitations in instrumentation combined with the unfortunate combination of very noisy data and the severe ill-posedness of the inverse problem have been (and still are) responsible for the slow dissemination of ET as a reliable structure determination technique in life sciences. The former issue is partly addressed by the rapid technological development, so we focus on the latter, which is due to the following reasons.

The dose problem. This is *the* single most important problem in ET. It limits the total number of images that can be taken and arises due to specimen damage during electron exposure. A typical range of dose that can be tolerated by a biological specimen is about 2000–7000 $\mathrm{e}^-/\mathrm{nm}^2$, which translates into about a total of 500–1250 $\mathrm{e}^-/\mathrm{pixel}$ (at $25000\times$ magnification with pixel size of $14\ \mu\mathrm{m}$) distributed over 60 or 120 micrographs, so each micrograph is very noisy, and the Poisson randomness of the data (shot noise) has to be accounted for.

Limited range of the tilt angle. Restrictions in the data acquisition geometry for ET, especially the restriction on the range of the tilt angle in single-axis tilting, lead to limited angle data and therefore imply that the conditions for stable reconstruction are not fulfilled.

Region of interest problem. For a given positioning of the specimen, only a subregion of it is subject to electron exposure. Thus, the region of interest then equals (or is a subset of) the intersection of all the exposed parts of the specimen from different positions. Since we have contribution from outside the region of interest,[1] we are dealing with the region of interest problem (local tomography), somewhat similar to the well-known "long object problem" in three-dimensional CT.

2.3. The inverse problem in ET. We therefore confine ourselves to presenting a very brief outline for how one arrives at the expression for the forward operator that occurs in the standard phase contrast model used by the ET community. The interested reader is referred to [4, 10, 23] for a more detailed exposition.

The starting point is to assume that we have perfect coherent imaging; i.e., the incoming electron wave is a monochromatic plane wave (coherent illumination), and electrons scatter only elastically. The scattering properties of the specimen are in this case given by the electrostatic potential, and the electron-specimen interaction is modeled by the scalar Schrödinger equation. The picture is completed by adding a description of the effects of the optics and the detector of the TEM, both modeled as convolution operators. However, inelastic scattering and incoherent illumination introduce partial incoherence, so the basic assumption of perfect coherent imaging must be relaxed. The incoherence that stems from inelastic scattering is accounted for within the coherent framework by introducing an imaginary part to the scattering potential, called the absorption potential. The incoherence that stems from incoherent illumination is modeled by modifying the convolution kernel that describes the effect of the optics. Next, as shown in [4, Theorem 9.5], taking the first order Born approximation and linearizing the intensity enables one to explicitly express the measured intensity in terms of the propagation operator (well known from diffraction tomography [18, p. 48]) acting on the scattering potential of the specimen convolved with point spread functions describing the optics and detector. The *standard phase contrast model* used by the ET community for the image formation in TEM is based on replacing the propagation operator by its high energy limit as the wave number tends to infinity. This yields a model for the image formation that is based on the parallel beam transform (see (2.3) for a definition).

The structure of the specimen is assumed to be fully described by the *scattering potential* $f\colon \mathbb{R}^3 \to \mathbb{C}$, which is defined as

$$(2.1) \qquad f(\boldsymbol{x}) := -\frac{2m}{\hbar^2}\big(V(\boldsymbol{x}) + iV_{\mathrm{abs}}(\boldsymbol{x})\big),$$

---

[1]The exposed part of the specimen is larger than the region of interest.

where m denotes the electron mass at rest, $V \colon \mathbb{R}^3 \to \mathbb{R}^-$ is the potential energy[2] that models elastic interaction, and $V_{\mathrm{abs}} \colon \mathbb{R}^3 \to \mathbb{R}^-$ is the absorption potential that models the decrease in the flux, due to inelastic scattering, of the nonscattered and elastically scattered electrons. Under the assumptions and approximations outlined in the previous paragraph, the expression for the *intensity generated by a single electron* is given as

$$(2.2)\quad \mathcal{I}(f)(\boldsymbol{z},\boldsymbol{\omega}) := \frac{1}{M^2}\left(1 - (2\pi)^{-2}\left[\left\{\mathrm{PSF}^{\mathrm{re}}(\cdot,\boldsymbol{\omega}) \underset{\boldsymbol{\omega}^\perp}{\circledast} \mathcal{P}(f^{\mathrm{re}})(\cdot,\boldsymbol{\omega})\right\}\left(\frac{\boldsymbol{z}}{M}\right)\right.\right.$$

$$\left.\left. + \left\{\mathrm{PSF}^{\mathrm{im}}(\cdot,\boldsymbol{\omega}) \underset{\boldsymbol{\omega}^\perp}{\circledast} \mathcal{P}(f^{\mathrm{im}})(\cdot,\boldsymbol{\omega})\right\}\left(\frac{\boldsymbol{z}}{M}\right)\right]k^{-1}\right)$$

for a unit vector $\boldsymbol{\omega} \in S^2$ and $\boldsymbol{z} \in \boldsymbol{\omega}^\perp$, where $\boldsymbol{\omega}^\perp := \left\{\boldsymbol{x} \in \mathbb{R}^n \mid \boldsymbol{x}\cdot\boldsymbol{\omega} = 0\right\}$. In the above expression, $f^{\mathrm{re}}, f^{\mathrm{im}} \colon \mathbb{R}^3 \to \mathbb{R}^+$ denotes the real and imaginary parts of f in (2.1) and $\mathcal{P}$ denotes the *parallel beam transform (X-ray transform)*, which is defined as the operator taking the line integral of a function, i.e.,

$$(2.3)\qquad \mathcal{P}(f)(\boldsymbol{y},\boldsymbol{\omega}) := \int_{t=-\infty}^{\infty} f(\boldsymbol{y} + t\boldsymbol{\omega})\,dt \quad \text{for } \boldsymbol{\omega} \in S^2 \text{ and } \boldsymbol{y} \in \boldsymbol{\omega}^\perp.$$

Moreover, $\circledast_{\boldsymbol{\omega}^\perp}$ denotes the two-dimensional convolution in the $\boldsymbol{\omega}^\perp$-plane, and the point spread functions $\mathrm{PSF}^{\mathrm{re}}$ and $\mathrm{PSF}^{\mathrm{im}}$ in (2.2) model the effect of the optics and incoherent illumination of the TEM. A precise expression for these can be found, e.g., in [4, section 9.1], [10, Chapter 65], or [23, section 3.3]. Finally, k is the particle wave number[3] w.r.t. the homogeneous background medium (which in our case is a vacuum) and M denotes the magnification.

As already mentioned, (2.2) yields the expression for the intensity generated by a single electron. The expression for the actual data measured on a micrograph needs to account for the detector point spread function (usually a slow-scan CCD camera) as well as the stochasticity in the data. Following [4, section 6.3], the stochasticity in the data is captured by assuming that the actual data delivered by the detector from a pixel should be modeled as a *sample of a random variable*, which in turn implies that the inverse problem in ET must be defined in a probabilistic setting.

DEFINITION 2.1. *We have a fixed finite set S_0 of directions on a smooth curve $S \subset S^2$ that defines our parallel beam data collection geometry. The scattering properties of the specimen are assumed to be fully described by the complex valued scattering potential f defined in (2.1). For each direction $\boldsymbol{\omega} \in S_0$, the specimen is probed by a monochromatic wave, and the resulting data on the micrograph at pixel (i,j) is denoted by $\mathrm{data}[f](\boldsymbol{\omega})_{i,j}$. The forward operator in ET, denoted by $\mathcal{T}$, is defined as the expected value of $\mathrm{data}[f](\boldsymbol{\omega})_{i,j}$, i.e.,*

$$\mathcal{T}(f)(\boldsymbol{\omega})_{i,j} := \mathbf{E}\left[\mathrm{data}[f](\boldsymbol{\omega})_{i,j}\right] \quad \textit{for } \boldsymbol{\omega} \in S^2 \textit{ and pixel } (i,j).$$

The inverse problem is to determine f when a sample of $\mathrm{data}[f](\boldsymbol{\omega})_{i,j}$ is known for $\boldsymbol{\omega} \in S_0$ and finitely many pixels (i,j).

---

[2] The potential energy is related to the electrostatic potential $U \colon \mathbb{R}^3 \to \mathbb{R}^+$ by $V = -eU$, where e is the charge of the electron.

[3] We use the convention that the relation between the wave number k and the wavelength λ is given by $k = 2\pi/\lambda$.

The full expression for $\mathrm{data}[f](\boldsymbol{\omega})_{i,j}$ (and the corresponding forward operator $\mathcal{T}$) is given in [4, equation (29)]. We will settle for a simplified version, also given in [4, equation (30)], which yields the following expression for the forward operator:

$$(2.4) \qquad \mathcal{T}(f)(\boldsymbol{\omega})_{i,j} = \mathrm{gain}_{i,j} \, |\triangle_{i,j}| \, \mathrm{Dose}(\boldsymbol{\omega}) \Big\{ \mathrm{PSF}_{\mathrm{det}} \underset{\boldsymbol{\omega}^\perp}{\circledast} \mathcal{I}(f)(\cdot, \boldsymbol{\omega}) \Big\}(\boldsymbol{z}_{i,j}) + \epsilon_{i,j}.$$

In the above expression, $\mathrm{gain}_{i,j}$ is a detector constant, $|\triangle_{i,j}|$ is the area of the (i,j)th pixel, $\mathrm{Dose}(\boldsymbol{\omega})$ is the incoming dose which gives the number of electrons hitting the specimen per area unit, $\mathrm{PSF}_{\mathrm{det}}$ is the detector point spread function, and $\epsilon_{i,j}$ is the mean value of the stochastic variable representing the *additive noise introduced by the detector*.

2.4. Integral geometric approaches for solving the inverse problem. There are two main assumptions underlying all current integral geometric approaches for solving the inverse problem given in Definition 2.1. The first is to assume that *the forward operator yields the actual measured data*; i.e., the data in pixel (i,j) in the micrograph with tilt $\boldsymbol{\omega}$ equals the expected value of the random variable $\mathrm{data}[f](\boldsymbol{\omega})_{i,j}$. The second is to assume that *the forward operator is given by* (2.4). Next, we shall see that appropriate postprocessing of the measured data allows us to obtain an expression for the values of the parallel beam transform on $(\boldsymbol{z}_{i,j}, \boldsymbol{\omega})$ with $\boldsymbol{\omega} \in S_0$ and $\boldsymbol{z}_{i,j} \in \Sigma \subset \boldsymbol{\omega}^\perp$, where Σ is a fixed finite set defined by the pixels in the detector. We have in this way recast the inverse problem in ET (given by Definition 2.1) as the problem of inverting the parallel beam transform.

2.4.1. Generate single electron intensity data. The first step is to generate *single electron intensity data* from the actual measured data. This can be done by deconvolving the effects of the detector point spread function $\mathrm{PSF}_{\mathrm{det}}$ and rescaling the measured data so that it corresponds to the intensity generated by a *single electron*. Let $\mathrm{I}(\boldsymbol{\omega})_{i,j}$ correspond to the intensity generated by a single electron at pixel (i,j). If the rescaling and deconvolution are appropriately[4] done, then we get

$$\mathrm{I}(\boldsymbol{\omega})_{i,j} \approx \mathcal{I}(f)(\boldsymbol{z}_{i,j}, \boldsymbol{\omega}) \quad \text{for } \boldsymbol{\omega} \in S_0 \text{ and } \boldsymbol{z}_{i,j} \in \Sigma.$$

By (2.2), for $\boldsymbol{z}_{i,j} \in \Sigma$ we then get that

$$(2.5) \quad \Big\{ \mathrm{PSF}^{\mathrm{re}}(\cdot, \boldsymbol{\omega}) \underset{\boldsymbol{\omega}^\perp}{\circledast} \mathcal{P}(f^{\mathrm{re}})(\cdot, \boldsymbol{\omega}) \Big\} \Big(\frac{\boldsymbol{z}_{i,j}}{M} \Big)$$
$$+ \Big\{ \mathrm{PSF}^{\mathrm{im}}(\cdot, \boldsymbol{\omega}) \underset{\boldsymbol{\omega}^\perp}{\circledast} \mathcal{P}(f^{\mathrm{im}})(\cdot, \boldsymbol{\omega}) \Big\} \Big(\frac{\boldsymbol{z}_{i,j}}{M} \Big) \approx (2\pi)^2 k \Big(1 - M^2 \, \mathrm{I}(\boldsymbol{\omega})_{i,j} \Big).$$

One can now proceed in a number of different ways in order to recast the inverse problem in Definition 2.1 as the problem of inverting the parallel beam transform.

2.4.2. Amplitude contrast only. The easiest approach is to assume that we have *perfect optics (no defocus and no spherical or chromatic aberration) and ignore all apertures*. These assumptions imply that $\mathrm{PSF}^{\mathrm{re}} \equiv 0$ and $\mathrm{PSF}^{\mathrm{im}} = \delta_{\boldsymbol{\omega}^\perp}$ (see, e.g., [4, section 9.3]), so (2.5) reduces to

$$(2.6) \qquad \mathcal{P}(f^{\mathrm{im}}) \Big(\frac{\boldsymbol{z}_{i,j}}{M}, \boldsymbol{\omega} \Big) \approx (2\pi)^2 k \Big(1 - M^2 \, \mathrm{I}(\boldsymbol{\omega})_{i,j} \Big) \quad \text{for } \boldsymbol{z}_{i,j} \in \Sigma.$$

---

[4]The deconvolution of the detector point spread function $\mathrm{PSF}_{\mathrm{det}}$ needed to create $\mathrm{I}(\boldsymbol{\omega})$ is an ill-posed operation, and therefore it needs to be performed using a regularization scheme. However, the ill-posedness is not severe since the Fourier transform of $\mathrm{PSF}_{\mathrm{det}}$ is positive [4, Remark 6.3], so it should be fairly straightforward to perform this regularization as exemplified in [32].

The inverse problem in Definition 2.1 can now be reformulated as the problem of inverting the parallel beam transform of f^{im} when the data is given by the right-hand side of (2.6).

Note that the real part f^{re} of the scattering potential is absent in (2.6) and thus cannot be recovered. This is to be expected since the phase contrast is visible only due to the imperfections in the optics (with nonzero defocus and/or nonzero aberration). The inability to recover f^{re} is a serious deficiency with this approach since f^{re} is the part of the scattering potential that has a straightforward physical interpretation in terms of the molecular structure of the specimen, whereas f^{im} is a phenomenological construction that accounts for the decrease in the flux, due to inelastic scattering, of the nonscattered and elastically scattered electrons. Assuming only amplitude contrast therefore works well only with strongly scattering specimens where most of the contrast in the micrographs is from amplitude contrast.

2.4.3. Constant amplitude contrast ratio. This is the most common approach in ET. It is based on introducing an additional assumption, namely, that $f^{\mathrm{im}}(\boldsymbol{x}) = Q f^{\mathrm{re}}(\boldsymbol{x})$, where the constant Q is called the *amplitude contrast ratio*. Under this assumption (2.5) reduces to

$$(2.7) \quad \left\{ \mathrm{PSF}(\cdot, \boldsymbol{\omega}) \underset{\boldsymbol{\omega}^{\perp}}{\circledast} \mathcal{P}(f^{\mathrm{re}})(\cdot, \boldsymbol{\omega}) \right\} \left(\frac{\boldsymbol{z}_{i,j}}{M} \right) \approx (2\pi)^2 k \left(1 - M^2 \, \mathrm{I}(\boldsymbol{\omega})_{i,j} \right) \quad \text{for } \boldsymbol{z}_{i,j} \in \Sigma,$$

where

$$\mathrm{PSF}(\boldsymbol{z}, \boldsymbol{\omega}) := \left\{ \mathrm{PSF}^{\mathrm{re}}(\cdot, \boldsymbol{\omega}) + Q \, \mathrm{PSF}^{\mathrm{im}}(\cdot, \boldsymbol{\omega}) \right\}(\boldsymbol{z}).$$

An expression for $\mathcal{P}(f^{\mathrm{re}})\left(\frac{\boldsymbol{z}_{i,j}}{M}, \boldsymbol{\omega} \right)$ can now be obtained by deconvolving the point spread function PSF in the expression (2.7).

There are several problems with this above approach. The first is that it requires a priori knowledge of Q. Second, deconvolving PSF is an ill-posed operation. This ill-posedness is especially pronounced since the Fourier transform of the kernel PSF has multiple zeroes (see, e.g., [4, section 9.1]). Thus, if one wants to use (2.7) in order to retrieve f^{re} (and f^{im} with knowledge of Q), then one needs to regularize the deconvolution operation involved in the right-hand side of (2.7). The most common approach is to again assume perfect optics and ignore all apertures. However, in such a case the criticism raised against the amplitude contrast model (2.6) also applies to this case, and not much is gained.

2.4.4. Phase contrast model with low-resolution amplitude contrast. We now propose a novel approach that does circumvent some of the difficulties raised above. The idea is to recover f^{re} by a hybrid approach. Begin by assuming *perfect optics (no defocus and no spherical or chromatic aberration) and ignore all apertures*. Under these assumptions we know that (2.6) is valid, which gives an expression for $\mathcal{P}(f^{\mathrm{im}})\left(\frac{\boldsymbol{z}_{i,j}}{M}, \boldsymbol{\omega} \right)$ with $\boldsymbol{z}_{i,j} \in \Sigma$. Inserting this expression into (2.5) yields an expression for

$$\left\{ \mathrm{PSF}^{\mathrm{re}}(\cdot, \boldsymbol{\omega}) \underset{\boldsymbol{\omega}^{\perp}}{\circledast} \mathcal{P}(f^{\mathrm{re}})(\cdot, \boldsymbol{\omega}) \right\} \left(\frac{\boldsymbol{z}_{i,j}}{M} \right).$$

Finally, by deconvolving the point spread function $\mathrm{PSF}^{\mathrm{re}}$, we obtain the expression for $\mathcal{P}(f^{\mathrm{re}})\left(\frac{\boldsymbol{z}_{i,j}}{M}, \boldsymbol{\omega} \right)$ with $\boldsymbol{z}_{i,j} \in \Sigma$. This deconvolution operation is, however, ill-posed since the Fourier transform of the corresponding kernel $\mathrm{PSF}^{\mathrm{re}}$ has multiple zeroes. Hence, in order to use this approach, one needs to regularize this deconvolution operation.

2.4.5. Phase contrast model with higher order terms. The troublesome deconvolutions with the optics point spread functions can be avoided altogether if one makes an approximation based on the asymptotic expansion of the forward operator that includes higher order terms. More precisely, in [4, equation (40)] it is shown that

$$\mathcal{I}(f)(\boldsymbol{z}, \boldsymbol{\omega}) = \frac{1}{M^2}\Bigg(1 - (2\pi)^{-2}\mathcal{P}(f^{\text{im}})\Big(\frac{\boldsymbol{z}}{M}, \boldsymbol{\omega}\Big)k^{-1}$$
$$+ (2\pi)^{-2}\bigg\{\Big(\frac{\triangle z}{2} + q\Big)\triangle_{\boldsymbol{\omega}^\perp}\Big[\mathcal{P}(f^{\text{re}})(\cdot, \boldsymbol{\omega})\Big]\Big(\frac{\boldsymbol{z}}{M}\Big)$$
$$+ \triangle_{\boldsymbol{\omega}^\perp}\bigg[\int_{\mathbb{R}} s f^{\text{re}}(s\boldsymbol{\omega} + \cdot)\,ds\bigg]\Big(\frac{\boldsymbol{z}}{M}\Big)\bigg\}k^{-2}\Bigg) + O(k^{-3}),$$

where $\triangle_{\boldsymbol{\omega}^\perp}$ is the two-dimensional Laplacian in the $\boldsymbol{\omega}^\perp$-plane, $\triangle z$ is the defocus, and q is the shortest distance (considering all the tilts) between the specimen and the objective lens in the idealized optical system (the value of q is determined by the magnification M and focal length of the objective lens [4, section 8.5]). Now, note that

$$\int_{\mathbb{R}} s f^{\text{re}}(s\boldsymbol{\omega} + \boldsymbol{z})\,ds \approx q\mathcal{P}(f^{\text{re}})(\boldsymbol{z}, \boldsymbol{\omega}),$$

which holds simply because q is much larger than the specimen thickness (where f^{re} has its support). Moreover, $\triangle_{\boldsymbol{\omega}^\perp}\big[\mathcal{P}(f^{\text{re}})(\boldsymbol{z}, \boldsymbol{\omega})\big] = \mathcal{P}(\triangle f^{\text{re}})(\boldsymbol{z}, \boldsymbol{\omega})$, where $\triangle$ is the Laplacian in $\mathbb{R}^3$, so we therefore end up with the following replacement of (2.5):

$$(2.8) \quad \mathcal{P}(f^{\text{im}})\Big(\frac{\boldsymbol{z}_{i,j}}{M}, \boldsymbol{\omega}\Big) + \Big(\frac{\triangle z}{2} + 2q\Big)k^{-1}\mathcal{P}(\triangle f^{\text{re}})\Big(\frac{\boldsymbol{z}_{i,j}}{M}, \boldsymbol{\omega}\Big)$$
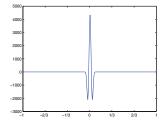$$\approx (2\pi)^2 k\Big(1 - M^2\,\mathrm{I}(\boldsymbol{\omega})_{i,j}\Big)$$

for $\boldsymbol{z}_{i,j} \in \Sigma$. One can now repeat the postprocessing approaches described in sections 2.4.3 and 2.4.4 but this time based on (2.8) instead of (2.5). This would yield postprocessing operations of data where one does not have to go through the ill-posed operation of deconvolving the optics.

2.4.6. Summary. As we have seen in the previous sections, performing a number of approximations allows us to recast the inverse problem in ET (given as in Definition 2.1) as the problem of solving (2.5) for f^{re} and f^{im}. This problem can then by additional assumptions be reduced to the problem of inverting the X-ray transform. Finally, bearing in mind the data collection scheme outlined in Definition 2.1, we are reduced to inverting the parallel beam transform since the line complex where the X-ray transform is sampled consists of lines parallel to a direction (which in turn varies on a curve in S^2).

3. Limited data local tomography. To help the reader understand our three-dimensional local reconstruction methods, we will first outline planar Lambda tomography and then recall the parameterization of lines for the ET data set in $\mathbb{R}^3$.

Lambda tomography [6, 5, 28] is a very clever algorithm for parallel beam or fan beam tomography in the plane. It allows one to image a function $f(\boldsymbol{x})$ using only line integrals of f for lines near $\boldsymbol{x}$. It is a variant of the standard filtered backprojection inversion algorithm that replaces the standard filter (that has infinite support)

(a) Plot of the convolution kernel we use in place of $-D_\sigma^2$ (see (5.8)). The kernel is local because it is zero off of the interval $[-0.1, 0.1]$.

(b) Plot of the standard filtered backprojection kernel with a comparable width.

FIG. 1. *Plot of kernels in Lambda tomography and in filtered backprojection. We see that the Lambda kernel illustrated in Figure* 1(a) *is local, whereas the standard filtered backprojection kernel shown in Figure* 1(b) *has infinite support.*

with a filter that takes a second derivative in the detector variable. Because the numerical derivative filter has small support, just near the line being evaluated, this reconstruction becomes local; see Figure 1.

The formula reads as follows:

$$(3.1) \qquad \Lambda_\mu(f) = \frac{1}{4\pi} \mathcal{P}^* \big(\mu - \mathcal{D}_{\boldsymbol{\omega}^\perp}^2 \big) \mathcal{P}(f).$$

In the above formula, $\mathcal{P}^*$ is the standard dual parallel beam transform integrating over all lines in the plane through the given point and $\mathcal{D}_{\boldsymbol{\omega}^\perp}^2$ is the second derivative in the $\boldsymbol{\omega}^\perp$ direction, i.e.,

$$\mathcal{D}_{\boldsymbol{\omega}^\perp}^2 (g)(\boldsymbol{y}, \boldsymbol{\omega}) := \frac{d^2}{ds^2} g\big(\boldsymbol{y} + s\boldsymbol{\omega}^\perp, \boldsymbol{\omega}\big)\bigg|_{s=0} \qquad \text{for } \boldsymbol{y} \in \mathbb{R}^2$$

with $\boldsymbol{\omega} := (\sin\theta, \cos\theta)$ and $\boldsymbol{\omega}^\perp := (\cos\theta, -\sin\theta)$. In this section, $\boldsymbol{\omega}^\perp$ is a vector, and for the three-dimensional parallel beam transform, $\boldsymbol{\omega}^\perp$ is a plane. Note that $\boldsymbol{\omega}$ is the unit vector $\pi/2$ radians counterclockwise from $\boldsymbol{\omega}^\perp$.

We subtract $\mathcal{D}_{\boldsymbol{\omega}^\perp}^2$ in (3.1) so that the Fourier transform of the kernel of Λ_μ is positive. *The result is a reconstruction not of f but of a function $\Lambda_\mu(f)$ that has singularities at the same places as f but with the singularities accentuated.* As has been shown in numerous articles (e.g., [6, 16, 21]) and as we will try to show here, Lambda reconstructions can be as useful as reconstructions from filtered backprojection if one does not need actual density values or if one has only local data from which density values cannot be obtained. The constant $\mu \geq 0$ is included in (3.1), as suggested by Smith and coauthors [26, 6], to provide some contour to the reconstruction. That is, the backprojected second derivative

$$-\Delta\mathcal{P}^*\mathcal{P}(f) = \mathcal{P}^*\big(-\mathcal{D}_{\boldsymbol{\omega}^\perp}^2\mathcal{P}\big)(f) = \Lambda_0(f),$$

or "pure" Lambda, emphasizes density changes or boundaries. The μ factor provides "contours" from the smoothed version of the original function since it results in the convolution

$$\mu\mathcal{P}^*\mathcal{P}(f) = f * \frac{2\mu}{\|\cdot\|},$$

where $*$ denotes the convolution in $\mathbb{R}^3$. The sum, (3.1), provides a reconstruction including both contours of f and the boundaries. A more complete rationale and analysis are given in [6, 5].

We now recall the three-dimensional parallel beam complex for ET. Let $S \subset S^2$ be a smooth curve on the sphere, and for $\boldsymbol{\omega} \in S$ let $\boldsymbol{\omega}^\perp$ be the plane through the origin perpendicular[5] to $\boldsymbol{\omega}$. Then, following any of the approaches outlined in section 2.4, the inverse problem in ET as stated in Definition 2.1 can be recast as the problem of recovering f given values $\mathcal{P}(f)(\boldsymbol{y}, \boldsymbol{\omega})$, where $\mathcal{P}$ is given as in (2.3), $\boldsymbol{\omega} \in S$, and $\boldsymbol{y} \in \boldsymbol{\omega}^\perp$ (or for the local problem, $\boldsymbol{y}$ is in a proper subset of $\boldsymbol{\omega}^\perp$). The example below shows that this is an intrinsically ill-posed problem in the single-axis tilting case since the local transform is not injective even in the absence of noise. Thus, singularity detection algorithms such as Lambda tomography are natural methods since they regularize the problem by reconstructing only features that are stably visible (see, e.g., [20, 16, 21]).

EXAMPLE 3.1. *Assume $f(x) = g(x_3)$, where the specimen is parallel to the (x_1, x_2)-plane. Then, only $\int_{-\infty}^{\infty} g(x_3)\, dx_3$ can be determined from single-axis tilt ET data with tilt angle less than $\pi/2$. This also is a counterexample for any set of lines, as in ET, without horizontal directions.*

4. The algorithm in general. In this section, we describe our Lambda tomography algorithm for directions (or angles) on an arbitrary smooth curve $S \subset S^2$. Note that we follow an ET convention when we use the word "angle" to describe a point on S^2. This general setup will provide a general framework for the single-axis tilt geometry we use in ET, which will be described in section 5. The algorithm is general enough to take care of other tilting geometries such as dual-axis and conical tilting, which some of the newest electron microscopes can provide. A generalization of algorithm to slant-hole SPECT (with the same geometry as conical tilt) will be given in [22].

The planar Lambda tomography we described in section 3 has two important advantages: it solves the region of interest problem—it is local—and it is easily adaptable to other limited data sets in the plane [16, 21]. As noted in section 1, the inverse problem in ET (as given in Definition 2.1) can be rephrased as a three-dimensional limited angle region of interest reconstruction problem. It is therefore natural to consider a type of singularity detection algorithm related to Lambda tomography. Furthermore, as shown by Example 3.1, *inversion is not possible, so recovering singularities is an appropriate goal.* It also turns out that, despite the severe ill-posedness of the inverse problem, *those singularities that can be recovered are recovered stably* at least in range of Sobolev spaces.[6] Such an algorithm includes two pieces, a backprojection operator and a derivative along the lines.

Let S be a curve on the sphere. The backprojection operator is the *dual parallel beam transform* for directions on the curve S,

$$(4.1) \qquad \mathcal{P}_S^*(g)(\boldsymbol{x}) := \int_{\boldsymbol{\omega} \in S} g\big(\boldsymbol{x} - (\boldsymbol{x} \cdot \boldsymbol{\omega})\boldsymbol{\omega}, \boldsymbol{\omega}\big)\, d\boldsymbol{\omega} \quad \text{for } \boldsymbol{x} \in \mathbb{R}^3,$$

where the measure $d\boldsymbol{\omega}$ is the arc length measure on the curve S and the point $\boldsymbol{x} - (x \cdot \boldsymbol{\omega})\boldsymbol{\omega}$ is the projection of $\boldsymbol{x}$ onto the plane $\boldsymbol{\omega}^\perp$.

---

[5] Note that $\boldsymbol{\omega}^\perp$ was a direction in S^1 perpendicular to $\boldsymbol{\omega}$ in the planar (two-dimensional) setting, whereas in the three-dimensional setting it is a plane perpendicular to $\boldsymbol{\omega}$.

[6] A stronger type of stability would be a microlocal inverse continuity estimate, and the authors are not aware of such a direct estimate for these operators.

The derivative along lines is defined as follows. Assume the curve S is parameterized by the differentiable function $\boldsymbol{\omega}(\theta)$ with derivative $\boldsymbol{\omega}'(\theta) \neq \mathbf{0}$, and let

$$(4.2) \qquad \boldsymbol{\sigma}(\theta) := \frac{\boldsymbol{\omega}'(\theta)}{\|\boldsymbol{\omega}'(\theta)\|}$$

be a unit tangent to the curve S at $\boldsymbol{\omega}(\theta)$. Then, we denote the second derivative in direction $\boldsymbol{\sigma}$ by

$$(4.3) \qquad \mathcal{D}_{\boldsymbol{\sigma}}^2 g(\boldsymbol{y}, \boldsymbol{\omega}(\theta)) := \frac{d^2}{ds^2} g(\boldsymbol{y} + s\boldsymbol{\sigma}(\theta), \boldsymbol{\omega}(\theta)) \Big|_{s=0}.$$

Our basic reconstruction operator is

$$(4.4) \qquad \mathcal{L}(f) := \mathcal{P}_S^* \big((\mu - \mathcal{D}_{\boldsymbol{\sigma}}^2) \mathcal{P}(f) \big).$$

This is a natural generalization of the two-dimensional Lambda operator (3.1) since it includes a second derivative along lines, a smoothing term, and a backprojection. We include the factor of μ, as is done for standard Lambda tomography, to provide contour to the reconstruction.

How $\mathcal{L}$ detects singularities can be understood using microlocal analysis, as we do in section 6. We will show that $\mathcal{L}$ is a pseudodifferential operator (PDO) with a mildly singular symbol (Theorem A.1). Moreover, ET data are very noisy, as discussed in section 2.2, so to cope with that we smooth in two ways. First, we evaluate the derivative $\mathcal{D}_{\boldsymbol{\sigma}}^2$ using a kernel that is a smoothed version of the second derivative. Second, we smooth by averaging nearby slices; that is, we also convolve in the $\boldsymbol{\omega}^\perp$-plane in the direction perpendicular to $\boldsymbol{\sigma}$. We will describe this smoothing explicitly in the case of single-axis tilting in the next section.

5. Single-axis tilt ET. In this section, we will describe our algorithm for single-axis tilt ET. In *single-axis tilt* ET, one restricts the directions to a single tilt axis. We use a coordinate system where the electrons come in along the z-axis when $\boldsymbol{\omega} = (0,0,1)$, and we assume the *tilt axis* is the x-axis. Let us now write (4.4) in these coordinates.

Expression for S. Because the specimen cannot be fully rotated, this means that the curve of directions, S, is an arc of a circle in the (y, z)-plane and there is a limited angular range of $\pm\theta_{\max}$, where $\theta_{\max} \approx \pi/3$ radians. One appropriate parameterization for the curve S in this setting is

$$(5.1) \qquad \boldsymbol{\omega}(\theta) := (0, \sin\theta, \cos\theta), \quad \theta \in \,]{-\theta_{\max}}, \theta_{\max}[,$$

and by (4.2) we get

$$(5.2) \qquad \boldsymbol{\sigma}(\theta) = (0, \cos\theta, -\sin\theta).$$

Expression for $\mathcal{P}$. Now, $\boldsymbol{e}_1 := (1, 0, 0)$ and $\boldsymbol{\sigma}(\theta)$ form an orthonormal basis of the plane $\boldsymbol{\omega}(\theta)^\perp$ and thereby provide orthonormal coordinates on $\boldsymbol{\omega}(\theta)^\perp$:

$$(5.3) \qquad \boldsymbol{y} = (y_1, y_{\boldsymbol{\sigma}}) \mapsto y_1 \boldsymbol{e}_1 + y_{\boldsymbol{\sigma}} \boldsymbol{\sigma}(\theta) \in \boldsymbol{\omega}(\theta)^\perp.$$

In these coordinates the set of lines is parameterized by

$$(5.4) \qquad \begin{aligned} Y &:= \Big\{ (\boldsymbol{y}, \theta) \mid \boldsymbol{y} = (y_1, y_{\boldsymbol{\sigma}}) \in \mathbb{R}^2, \, \theta \in \,]{-\theta_{\max}}, \theta_{\max}[\Big\}, \\ (\boldsymbol{y}, \theta) &\mapsto \ell(\boldsymbol{y}, \theta) := \Big\{ y_1 \boldsymbol{e}_1 + y_{\boldsymbol{\sigma}} \boldsymbol{\sigma}(\theta) + t\boldsymbol{\omega}(\theta) \mid t \in \mathbb{R} \Big\}, \end{aligned}$$

and functions on lines will be written $g(\boldsymbol{y}, \theta) = g\big((y_1, y_{\boldsymbol{\sigma}}), \theta\big)$, so in particular $\mathcal{P}$ has parameterization

$$(5.5) \qquad \mathcal{P}(f)(\boldsymbol{y}, \theta) := \mathcal{P}(f)\big(y_1 \boldsymbol{e}_1 + y_{\boldsymbol{\sigma}} \boldsymbol{\sigma}(\theta), \boldsymbol{\omega}(\theta)\big).$$

Expression for $\mathcal{P}_S^*$. Before expressing the dual operator $\mathcal{P}_S^*$ in (4.1) in these coordinates, we smooth it slightly in order to make it a classical Fourier integral operator (FIO) and in order to increase the accuracy in the numerical integration. This is done by choosing $0.9\,\theta_{\max} < \theta_{\mathrm{cut}} < \theta_{\max}$ and defining the smooth function

$$(5.6) \qquad \varphi : [-\pi/2, \pi/2] \to [0, 1], \quad \operatorname{supp}\varphi = [-\theta_{\mathrm{cut}}, \theta_{\mathrm{cut}}],$$

where φ is nonzero on $]{-}\theta_{\mathrm{cut}}, \theta_{\mathrm{cut}}[$ and equal to one on most of this interval. φ is then extended $\mathbb{R}$ by making it π-periodic. The *smoothed limited angle dual parallel beam transform*, which is the version of $\mathcal{P}_S^*$ that we will be using, is

$$(5.7) \qquad \mathcal{P}_{\theta_{\mathrm{cut}}}^*(g)(\boldsymbol{x}) := \int_{-\theta_{\mathrm{cut}}}^{\theta_{\mathrm{cut}}} g\Big(\boldsymbol{x} - \big(\boldsymbol{x} \cdot \boldsymbol{\omega}(\theta)\big)\boldsymbol{\omega}(\theta), \boldsymbol{\omega}(\theta)\Big)\varphi(\theta)\,d\theta \quad \text{for } \boldsymbol{x} \in \mathbb{R}^3.$$

A simple trapezoidal rule integration, which corresponds to a specific choice of φ, works well in (5.7).

Expression for $\mathcal{D}_{\boldsymbol{\sigma}}^2$. In our coordinates $(\boldsymbol{y}, \theta)$, $\mathcal{D}_{\boldsymbol{\sigma}}^2$ becomes

$$(5.8) \qquad \mathcal{D}_{\boldsymbol{\sigma}}^2(g)(\boldsymbol{y}, \theta) := \frac{d^2}{ds^2} g\big((y_1, s), \theta\big)\Big|_{s=0}.$$

Expression for (4.4). Our expression for the Lambda operator $\mathcal{L}$ in (4.4) becomes

$$(5.9) \qquad \mathcal{L}(f) = \mathcal{P}_{\theta_{\mathrm{cut}}}^*\big((\mu - \mathcal{D}_{\boldsymbol{\sigma}}^2)\mathcal{P}(f)\big).$$

This operator is a two-dimensional limited angle Lambda operator in each fixed plane $\boldsymbol{x} = \text{constant}$ (compare with (3.1)).

Further smoothing. We actually use a smoothed version of the derivative $\mathcal{D}_{\boldsymbol{\sigma}}^2$ in the $\boldsymbol{\sigma}$ direction, and we also smooth between slices in the $\boldsymbol{e}_1$ direction. This can be understood as either a convolution/smoothing of the data in the data plane, $\boldsymbol{\omega}^\perp$, or as a convolution/smoothing of the final reconstruction, as we now explain. Let $\phi_1 \in \mathscr{C}_c^\infty(\mathbb{R})$ be even with $\int_{\mathbb{R}} \phi_1 = 1$ and $\phi_2 \in \mathscr{C}_c^\infty(\mathbb{R}^2)$ be radial with $\int_{\mathbb{R}^2} \phi_2 = 1$. Moreover, let $\widetilde{\phi}_2$ be the two-dimensional parallel beam transform of ϕ_2, and note that $\widetilde{\phi}_2$ is radial and independent of direction. Let $(\phi_1 \otimes \widetilde{\phi}_2)(x_1, x_2, x_3) = \phi_1(x_1)\widetilde{\phi}_2(x_2, x_3)$. Then, for $(\boldsymbol{y}, \theta) \in Y$ and data f with compact support,

$$(5.10) \qquad (\phi_1 \otimes \widetilde{\phi}_2) \underset{\boldsymbol{\omega}^\perp}{\circledast} \mathcal{P}(f)(\boldsymbol{y}, \theta) = \mathcal{P}\big((\phi_1 \otimes \phi_2) * f\big)(\boldsymbol{y}, \theta),$$

where $*$ denotes the convolution in $\mathbb{R}^3$ and $\underset{\boldsymbol{\omega}^\perp}{\circledast}$ is the convolution in the detector plane, $\boldsymbol{\omega}(\theta)^\perp$. Equation (5.10) is valid since $\mathcal{P}$ integrates only over lines perpendicular to $\boldsymbol{e}_1$ and ϕ_1 is a function only of x_1. Because $\mathcal{L}$ is a convolution operator (see Theorem A.1), it commutes with the convolution with $\phi_1 \otimes \phi_2$. This means that

$$(5.11) \qquad \big(\phi_1 \otimes \phi_2\big) * \mathcal{L}(f) = \mathcal{P}_{\theta_{\mathrm{cut}}}^*\Big[(\mu - \mathcal{D}_{\boldsymbol{\sigma}}^2)\big((\phi_1 \otimes \widetilde{\phi}_2) \underset{\boldsymbol{\omega}^\perp}{\circledast} \mathcal{P}(f)\big)\Big]$$

$$(5.12) \qquad\qquad = \mathcal{P}_{\theta_{\mathrm{cut}}}^*\Big[\phi_1 \underset{\boldsymbol{e}_1}{\circledast} \big((\mu\widetilde{\phi}_2 - \mathcal{D}_{\boldsymbol{\sigma}}^2\widetilde{\phi}_2) \underset{\boldsymbol{\sigma}}{\circledast} \mathcal{P}(f)\big)\Big],$$

where $\circledast_{\boldsymbol{e}_1}$ and $\circledast_{\boldsymbol{\sigma}}$ are one-dimensional convolutions in the $\boldsymbol{\omega}^\perp$-plane in the respective directions $\boldsymbol{e}_1$ and $\boldsymbol{\sigma}(\theta)$. So, our algorithm can be viewed as a smoothed version of $\mathcal{L}(f)$ (left-hand side of (5.11)), a smoothing of the data before applying $\mathcal{L}$ (right-hand side of (5.11)), or averaging over slices (the $\circledast_{\boldsymbol{e}_1}$ convolution in (5.12)) of a smoothed derivative (the $\circledast_{\boldsymbol{\sigma}}$ convolution in (5.12)).

6. Microlocal analysis applied to ET. We will now use microlocal analysis to analyze which singularities of a specimen are stably visible from single-axis tilt ET data.

Microlocal analysis allows one to rigorously define singularities of functions such as object boundaries. This is made precise by the wavefront set whose definition is our first task. Next, the theory of FIOs describes which singularities of a function are visible from its ET data. This correspondence follows from general theorems of Greenleaf and Uhlmann [8] about geodesic Radon transforms on admissible complexes, and the microlocal properties of this specific transform were examined by Boman and Quinto [2]. Here we will give a basic version of the microlocal regularity theorem which will allow us to characterize visible singularities. The complete version of the theorem will be presented in the appendix along with characterizations of $\mathcal{L}$ as a convolution PDO. In the appendix, we also introduce a generalization, $\mathcal{L}_\triangle$ (A.14), of an operator of Louis and Maaß. Our characterization will show the trade-offs between the operators; $\mathcal{L}_\triangle$ can add stronger singularities than $\mathcal{L}$. At the end of the section, we give an example that illustrates the predictions.

Before stating the formal definition of the wavefront set we need to deal with a technicality.

REMARK 6.1. *The wavefront set is typically defined as a subset of the cotangent bundle, because in this way it is invariant under diffeomorphisms. Furthermore, this is a natural way to describe wavefronts in general. Here is the identification for $\mathbb{R}^3$. For $\boldsymbol{x} \in \mathbb{R}^3$, the cotangent space $T_{\boldsymbol{x}}^*(\mathbb{R}^n)$ is the set of linear functionals on the tangent space $T_{\boldsymbol{x}}(\mathbb{R}^3)$, and $\boldsymbol{dx}_j$ is the dual covector to $\frac{\partial}{\partial x_j}$ ($j = 1, 2, 3$). This gives a canonical representation,*

$$\boldsymbol{\xi} \ni \mathbb{R}^3 \to \boldsymbol{\xi dx} := \xi_1 \boldsymbol{dx}_1 + \xi_2 \boldsymbol{dx}_2 + \xi_3 \boldsymbol{dx}_3.$$

The cotangent bundle, $T^*(\mathbb{R}^3)$, is the set $T^*(\mathbb{R}^3) := \{(\boldsymbol{x}, \boldsymbol{\xi dx}) \mid \boldsymbol{x} \in \mathbb{R}^3, \boldsymbol{\xi} \in \mathbb{R}^3\}$, where $(\boldsymbol{x}; \boldsymbol{\xi dx}) = (x_1, x_2, x_3; \xi_1 \boldsymbol{dx}_1 + \xi_2 \boldsymbol{dx}_2 + \xi_3 \boldsymbol{dx}_3)$.

Recall that $\mathscr{D}'(\mathbb{R}^3)$ is the set of all distributions, $\mathscr{S}'(\mathbb{R}^3)$ is the set of tempered distributions (dual space of $\mathscr{S}(\mathbb{R}^3)$), and $\mathscr{E}'(\mathbb{R}^3)$ is the space of compactly supported distributions. We are now ready to define the concept of a wavefront set.

DEFINITION 6.2 (see [19, p. 259]). *Let f be a distribution, $\boldsymbol{x}_0 \in \mathbb{R}^n$, and $\boldsymbol{\xi}_0 \in \mathbb{R}^n \setminus \{\boldsymbol{0}\}$. We then define the following:*
  1. *f is in $\mathscr{C}^\infty$ microlocally near $(\boldsymbol{x}_0, \boldsymbol{\xi}_0 \boldsymbol{dx})$ if and only if there is a cut-off function $\psi \in \mathscr{C}_c^\infty(\mathbb{R}^n)$ with $\psi(\boldsymbol{x}_0) \neq 0$ and a function u homogeneous of degree zero that is smooth on $\mathbb{R}^n \setminus \{\boldsymbol{0}\}$ with $u(\boldsymbol{\xi}_0) \neq 0$ such that the product $u(\cdot)\widehat{\psi f}(\cdot)$ is rapidly decreasing at ∞.[7] The $\mathscr{C}^\infty$ wavefront set of f, $\mathrm{WF}(f)$, is the complement of the set of $(\boldsymbol{x}_0; \boldsymbol{\xi}_0 \boldsymbol{dx})$ near which f is microlocally smooth.*
  2. *f is in $\mathscr{H}^\alpha$ microlocally near $(\boldsymbol{x}_0; \boldsymbol{\xi}_0 \boldsymbol{dx})$ if and only if there is a cut-off function $\psi \in \mathscr{C}_c^\infty(\mathbb{R}^n)$ with $\psi(\boldsymbol{x}_0) \neq 0$ and a function u homogeneous of*

---

[7]In our context, a function h is *rapidly decreasing at* ∞ if for each $k \in \mathbb{N}$ there is a $C > 0$ such that for all $\boldsymbol{x} \in \mathbb{R}^n$, $|h(\boldsymbol{x})| \leq C(1 + \|\boldsymbol{x}\|)^{-k}$. Sometimes one replaces the function u by an open cone U containing $\boldsymbol{\xi}_0$ on which $\widehat{\psi f}$ is rapidly decreasing at ∞.

degree zero and smooth on $\mathbb{R}^n \setminus \{\mathbf{0}\}$ and with $u(\boldsymbol{\xi}_0) \neq 0$ such that the product $u(\cdot)\widehat{\psi f}(\cdot) \in \mathscr{L}^2\big(\mathbb{R}^n, \big(1 + |\boldsymbol{\xi}|^2\big)^{\alpha}\big)$. The $\mathscr{H}^{\alpha}$ wavefront set of f, $\mathrm{WF}^{\alpha}(f)$, is the complement of the set of $(\boldsymbol{x}_0, \boldsymbol{\xi}_0 d\boldsymbol{x})$ near which f is microlocally in $\mathscr{H}^{\alpha}$.

For example, if f is one inside the unit disk and zero outside, then $\mathrm{WF}(f) = \mathrm{WF}^1(f)$ and they both consist of the covectors conormal to the boundary of the disk. In general, if $f : \mathbb{R}^3 \to \mathbb{R}$ is $\mathscr{C}^{\infty}$ except for jump singularities along smooth surfaces, then the $\mathscr{C}^{\infty}$ wavefront set of f consists of all the conormals to these surfaces of discontinuity.

Having defined the necessary concept of a wavefront set, we now turn our attention to our main theorem, which characterizes the singularities that are visible from single-axis tilt ET data.

THEOREM 6.3 (microlocal regularity theorem). *Let $f \in \mathscr{E}'(\mathbb{R}^3)$, $(y_1, y_{\boldsymbol{\sigma}}, \theta_0) = \boldsymbol{y} \in Y$, and let $\boldsymbol{\xi}_0 \in \boldsymbol{\omega}(\theta)^{\perp}$ be a nonzero vector where we write $\boldsymbol{\xi}_0 = \xi_1 \boldsymbol{e}_1 + \xi_{\boldsymbol{\sigma}} \boldsymbol{\sigma}(\theta)$. Finally, let $\boldsymbol{x}_0 \in \ell(y_1, y_{\boldsymbol{\sigma}}, \theta)$. If $\xi_{\boldsymbol{\sigma}} \neq 0$, then there is a corresponding covector in $T_{\boldsymbol{y}}^*(Y)$ such that $(\boldsymbol{x}_0, \boldsymbol{\xi}_0 d\boldsymbol{x}) \in \mathrm{WF}(f)$ if and only if this covector is in $\mathrm{WF}\big(\mathcal{P}(f)\big)$ (this correspondence is given in Theorem A.6). If we also assume that $\mathcal{P}(f)$ is $\mathscr{C}^{\infty}$ near $\boldsymbol{y}$, then $(\boldsymbol{x}_0, \boldsymbol{\xi}_0 d\boldsymbol{x}) \notin \mathrm{WF}(f)$.*

Note that $d\boldsymbol{x}_1$ is conormal to $\boldsymbol{\omega}(\theta)$ (and thus conormal to the line $\ell(\boldsymbol{y}, \theta)$ for all θ since $\boldsymbol{\omega}(\theta)$ is in the (y, z)-plane). So, the restriction $\xi_{\boldsymbol{\sigma}} \neq 0$ just means $\boldsymbol{\xi}_0 d\boldsymbol{x}$ defined in the theorem above is not a multiple of $d\boldsymbol{x}_1$ ($\boldsymbol{\xi}_0$ is not parallel to $\boldsymbol{e}_1$).

In general, Radon transforms (such as the parallel beam transform in this article) detect only singularities perpendicular to the sets of integration, so it is not surprising that the theorem provides information only about singularities of f conormal to $\boldsymbol{\omega}(\theta)$ since these are conormal to the corresponding lines in the data set. However, for this transform, there are two conormal directions that are excluded, $\boldsymbol{\xi}_0 = \pm \boldsymbol{e}_1$; these are *"bad" cotangent directions* because they "should" be visible (they are conormal to lines in the data set), but they cause problems. We will examine these problems in the appendix, and in particular we will show that $\mathcal{L}$ can add singularities in these directions.

EXAMPLE 6.4. *We now illustrate the implications of Theorem 6.3 for ET. Let D be the unit disk in space, and let f be one inside D and zero outside. Assume the region of interest contains D, and assume that φ satisfies (5.6). If $\boldsymbol{x} \in \mathrm{bd}\, D$, then $\boldsymbol{x}$ is normal to $\mathrm{bd}\, D$ at $\boldsymbol{x}$, so $(\boldsymbol{x}; \boldsymbol{x}d\boldsymbol{x}) \in \mathrm{WF}(f)$. No matter what θ_{cut} is, the wavefront $\pm\boldsymbol{e}_1 d\boldsymbol{x}$ is problematic. This is a conormal at the points $(\pm 1, 0, 0)$ on the boundary. Singularities in other conormal directions are visible from the data as long as the direction is perpendicular to a line in the data set. Let $\boldsymbol{x} = (x_1, x_2, x_3) \in \mathrm{bd}\, D$. Because of the geometry of the single-axis tilt (5.1), this means that $|x_3/x_2| < \tan(\theta_{\mathrm{cut}})$ in order for the wavefront at $\boldsymbol{x}$ to be visible. The part of the sphere that should be visible is illustrated in Figure 2. One would expect for numerical reasons that the boundary would get gradually less well defined near the edge of the visible part.*

7. Applications to real data. We have tested the limited angle Lambda algorithm based on the Lambda operator (5.9) on both in vitro and in situ ET data. The Lambda reconstruction is obtained by applying the limited angle Lambda algorithm directly on the region of interest. This reconstruction is compared to a filtered back-projection (FBP) reconstruction that has been regularized by an additional low-pass filtering (low-pass FBP). This latter filtering, which in our case reduces the resolution to 10 nm, is necessary in order to gain stability, and the value for the low-pass filtering represents the best trade-off between stability and resolution if FBP is to be used on
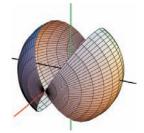
FIG. 2. *Part of sphere with normal vectors normal to lines in the data set with $\theta_{\mathrm{cut}} = 60°$.* *The x_1-axis is facing out of the page.*

these particular examples. The low-pass FBP is applied to the entire reconstruction region, and the region of interest is then extracted for comparison against the limited angle Lambda reconstruction.

The first case, shown in Figure 3, is the reconstruction of in vitro monoclonal immunoglobulin G (IgG) molecules with a molecular weight of 150 kDa. The ET data was collected from single-axis tilting (see section 2.1) with a uniform sampling of the tilt angle in $[-60°, 60°]$ at $1°$ step. The pixel size is 0.5241 nm and the total dose is 1820 $\mathrm{e}^-/\mathrm{nm}^2$. A detailed account on the background for the study, the experimental setting, and the study objective is given in [24]. The reconstruction region is $256 \times 256 \times 256$ pixels in size, and the local region of interest is centered in the midpoint of the reconstruction region with a size of $128 \times 128 \times 128$ pixels.
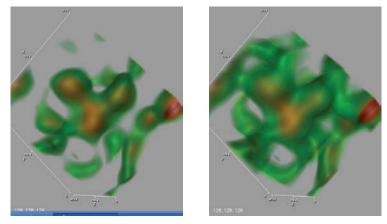
Figure 3 shows how the limited angle Lambda reconstruction emphasizes boundaries better. It also seems to somewhat suppress the background noise outside the molecule, and the IgG molecule (which is in the center) is more visible than in the low-pass FBP reconstruction.

The next case, shown in Figure 4, is the reconstruction of an in situ tissue sample (could be a human, rat, or mouse kidney). The ET data was collected from single-axis tilting (see section 2.1) with a uniform sampling of the tilt angle in $[-60°, 60°]$ at $2°$ step. The pixel size is 0.5241 nm and the total dose is 1520 $\mathrm{e}^-/\mathrm{nm}^2$. A detailed account on the background for the study, the experimental setting, and the study objective is given in [30, 27]. The reconstruction region is $300 \times 300 \times 150$ pixels in size, and the local region of interest is centered in the midpoint of the reconstruction region and is of $200 \times 200 \times 140$ pixels size.

Since the object in Figure 4 is in situ, parts of the object outside the region of interest will affect the FBP reconstruction in the region of interest but not the Lambda reconstruction (since it does not require data from outside the region of interest). The reconstructions in Figure 4 clearly show that the limited angle Lambda reconstruction defines boundaries better since the "V" shaped region containing the slit diaphragm (in the upper right side of the object) is more clearly defined than in the low-pass FBP reconstruction. This also illustrates the microlocal principles of section 6 since the slabs are tangent to lines in the data set.

Appendix. The microlocal properties of $\mathcal{P}$ and $\mathcal{L}$. In this section, we will describe the microlocal properties of our transform $\mathcal{P}$ and the reconstruction operator $\mathcal{L}$ (5.9). We will use this information to explain how the transform detects singularities and show the relevance to ET. The properties of the more general operator (4.4) are similar, and the details will be given in a subsequent article [22].
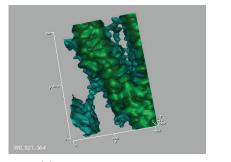
The convolution operator in $\mathbb{R}^n$ is denoted by $*$. For the Fourier transform on
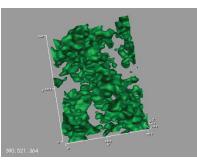
(a) Lambda reconstruction. (b) Low-pass FBP reconstruction.

FIG. 3. *The boundaries are better defined in the Lambda reconstruction when compared to the low-pass (10 nm-resolution) FBP reconstruction. The background noise is also suppressed. This makes the analysis of the IgG molecule easier.*

(a) Lambda reconstruction. (b) Low-pass FBP reconstruction.

FIG. 4. *The "V" shaped region containing the slit diaphragm is more clearly defined in the Lambda reconstruction than the low-pass (10 nm-resolution) FBP reconstruction.*

$\mathbb{R}^n$, we use the normalization

$$\mathcal{F}(f)(\boldsymbol{\xi}) = \widehat{f}(\boldsymbol{\xi}) := \int_{\boldsymbol{x}\in\mathbb{R}^n} e^{-i\boldsymbol{x}\cdot\boldsymbol{\xi}} f(\boldsymbol{x})\, d\boldsymbol{x}.$$

The two-dimensional Fourier transform on the plane $\boldsymbol{\omega}^\perp$ is defined in a similar way, and in the coordinates we chose for single axis tilt (see section 5), it is

$$\mathcal{F}_{\boldsymbol{\omega}^\perp}(g)(\boldsymbol{\eta},\theta) := \int_{(y_1,y_{\boldsymbol{\sigma}})\in\mathbb{R}^2} e^{-i(y_1,y_{\boldsymbol{\sigma}})\cdot(\eta_1,\eta_{\boldsymbol{\sigma}})} g(\boldsymbol{y},\theta)\, d\boldsymbol{y} \quad \text{for } \boldsymbol{\eta}\in\mathbb{R}^2.$$

Our next theorem characterizes the reconstruction operator as a convolution PDO with a symbol that is singular all along the ξ_1-axis. This has specific implications for reconstructions based on $\mathcal{L}$, as we explain in Theorem A.2 and Example A.5.

THEOREM A.1. *Let $\mathcal{P}^*_{\theta_{\mathrm{cut}}}$ be defined by (5.7), where the smooth function φ satisfies the assumptions given in (5.6), $\mathcal{P}$ is defined by (5.5), and $\mu \geq 0$. For $\boldsymbol{\xi} = (\xi_1,\xi_2,\xi_3) \in \mathbb{R}^3$, let $\boldsymbol{\xi}' = (\xi_2,\xi_3)$, and for $\boldsymbol{\xi}' \neq \boldsymbol{0}$, let $\arg(\boldsymbol{\xi}')$ be one of the*

angles in the plane from the ξ_2-axis to $\boldsymbol{\xi}'$.[8] Then, for $\mu \neq 0$ the operator $\mathcal{L}$ is defined for distributions of compact support. For $\mu = 0$, $\mathcal{L}$ is a continuous map from $\mathscr{H}^{\alpha+1}(\mathbb{R}^3)$ to $\mathscr{H}^{\alpha}(\mathbb{R}^3)$ for all $\alpha \in \mathbb{R}$. Moreover, in the coordinates defined above, $\mathcal{L}(f) = f * k$, and its symbol is the Fourier transform of k,

$$(\text{A.1}) \qquad \sigma(\boldsymbol{x}, \boldsymbol{\xi}) = \widehat{k}(\boldsymbol{\xi}) := \left(\frac{\varphi\big(\arg(\boldsymbol{\xi}') + \pi/2\big)}{(2\pi)^2 \|\boldsymbol{\xi}'\|} \right) (\mu + \|\boldsymbol{\xi}'\|^2).$$

Proof. To prove Theorem A.1, we need to show that

$$\mathcal{L}(f)(\boldsymbol{x}) = \frac{1}{(2\pi)^2} \int_{\boldsymbol{\xi} \in \mathbb{R}^3} e^{i\boldsymbol{x}\boldsymbol{\xi}} \, \widehat{k}(\boldsymbol{\xi}) \mathcal{F}(f)(\boldsymbol{\xi}) \, d\boldsymbol{\xi}, \quad \text{where } \widehat{k} \text{ is given by (A.1).}$$

Initially, we assume f is a smooth function of compact support, but by continuity in distribution space, the end results will be true for distributions of compact support, as we will explain when needed. We use the convention that if $\boldsymbol{x} = (x_1, x_2, x_3) \in \mathbb{R}^3$, then $\boldsymbol{x}' = (x_2, x_3)$, and we begin the calculations in the plane $x_1 = $ constant. It is straightforward to show using polar coordinates in this plane that

$$(\text{A.2}) \qquad \mathcal{P}^*_{\theta_{\text{cut}}} \mathcal{P}(f)(\boldsymbol{x}) = \int_{\boldsymbol{y}' \in \mathbb{R}^2} \frac{\varphi\big(\arg(\boldsymbol{y}')\big)}{\|\boldsymbol{y}'\|} f\big(\boldsymbol{x} + (0, \boldsymbol{y}')\big) \, dy'.$$

To write (A.2) as a PDO, we first fix x_1 and take the Fourier transform of (A.2) in $\boldsymbol{x}'$. Then, we use the fact about Fourier transforms of homogeneous functions [25, sect. 4, equation (7), p. 61] that the Fourier transform of $\varphi\big(\arg(\boldsymbol{y}')\big)/\|\boldsymbol{y}'\|$ is given by the first expression in parentheses in (A.1). To finish the proof, we take the inverse Fourier transform in x' and then the Fourier transform and inverse transform in x_1. This shows that

$$(\text{A.3}) \qquad \mathcal{P}^*_{\theta_{\text{cut}}} \mathcal{P}(f)(\boldsymbol{x}) = \frac{1}{(2\pi)^2} \int_{\boldsymbol{\xi} \in \mathbb{R}^3} e^{i\boldsymbol{x}\boldsymbol{\xi}} \left(\frac{\varphi\big(\arg(\boldsymbol{\xi}') + \pi/2\big)}{\|\boldsymbol{\xi}'\|} \right) \mathcal{F}(f)(\boldsymbol{\xi}) \, d\boldsymbol{\xi}.$$

Note that $\mathcal{P}^*_{\theta_{\text{cut}}} : \mathscr{E}'(Y) \to \mathscr{D}'(\mathbb{R}^3)$ is continuous, and a cutoff[9] applied to $\mathcal{P}$ is continuous from $\mathscr{E}'(\mathbb{R}^3)$ to $\mathscr{E}'(Y)$ by duality. These observations explain why $\mathcal{P}^*_{\theta_{\text{cut}}} \mathcal{P}$ and $\mathcal{L}$ are defined and continuous from $\mathscr{E}'(\mathbb{R}^3)$ to $\mathscr{D}'(\mathbb{R}^3)$.

To write $\mathcal{L}$ as a PDO, we first observe that, by an integration by parts, $D_\sigma^2 \mathcal{P}(f) = \mathcal{P}(\Delta_{\boldsymbol{x}'} f)$, where $\Delta_{\boldsymbol{x}'} = \frac{\partial^2}{\partial x_2^2} + \frac{\partial^2}{\partial x_3^2}$. This is clearly true for functions and true on $\mathscr{E}'$ by continuity. Then, we note that

$$(\text{A.4}) \qquad \mathcal{L}(f) = \mathcal{P}^*_{\theta_{\text{cut}}} \mathcal{P}\big((\mu - \Delta_{\boldsymbol{x}'})f\big),$$

so using (A.3) on $(\mu - \Delta_{\boldsymbol{x}'})f$ gives (A.1).

Finally, let $\mathcal{L}^0$ be defined as $\mathcal{L}$ with $\mu = 0$. The Sobolev continuity of $\mathcal{L}^0$ follows immediately from the calculation of its symbol above since the symbol of $\mathcal{L}^0$ is bounded above by $(1 + \|\xi\|^2)^{1/2}$ since $\|\xi'\| \leq \|\xi\|$ and $|\varphi|$ is bounded above by 1. This proves the Sobolev continuity of $\mathcal{L}^0$. Note that $\mathcal{L}$ is not defined on $\mathscr{H}^\alpha$ because of the singularity of $1/\|\boldsymbol{\xi}'\|$ at $\xi' = 0$. This concludes the proof of Theorem A.1. $\square$

---

[8]Note that $\varphi\big(\arg(\boldsymbol{\xi}')\big)$ is well defined since φ is π-periodic.
[9]Let ψ be a smooth function that is one on $[-\theta_{\text{cut}}, \theta_{\text{cut}}]$ and supported in $(-\theta_{\max}, \theta_{\max})$; then $\psi\mathcal{P} : \mathscr{E}'(\mathbb{R}^3) \to \mathscr{E}'(Y)$ is continuous, and $\mathcal{P}^*_{\theta_{\text{cut}}} \psi\mathcal{P} = \mathcal{P}^*_{\theta_{\text{cut}}} \mathcal{P}$.

We describe what $\mathcal{L}$ does to wavefront sets in our next theorem and in Example A.5.

THEOREM A.2. *Let $\mathcal{L}$ be as in Theorem* A.1*, and f is a distribution of compact support in the unit disk D. Finally, define*

(A.5) $\mathcal{V} := \left\{ (\boldsymbol{x}, \boldsymbol{\xi} \boldsymbol{dx}) \in T^*(\mathbb{R}^3) \setminus 0 \mid \xi_2 \neq 0, |\xi_3/\xi_2| < \tan\theta_{\text{cut}} \right\},$

(A.6) $\mathcal{A} := \left\{ (\boldsymbol{x}, \xi_1 \boldsymbol{dx}_1) \mid x_1 \in [-1, 1], \boldsymbol{x}' \in \mathbb{R}^2, \xi_1 \in \mathbb{R} \setminus 0 \right\}.$

Then,

(A.7) $\mathrm{WF}^\alpha\big(\mathcal{L}(f)\big) \cap \mathcal{V} = \mathrm{WF}^{\alpha+1}(f) \cap \mathcal{V},$

(A.8) $\mathrm{WF}^\alpha\big(\mathcal{L}(f)\big) \subset \big(\mathrm{WF}^{\alpha+1}(f) \cap \mathrm{cl}(\mathcal{V})\big) \cup \mathcal{A}.$

The set $\mathcal{V}$ in (A.5) is the set of "reliably visible" singularities. Equation (A.7) implies that singularities of f in those codirections are visible in the reconstruction $\mathcal{L}(f)$, and they are one order less smooth in Sobolev scale in the reconstruction than the corresponding singularities of f. Recall that visible covectors have to be conormal to lines in the data set by Theorem 6.3, and directions in $\mathcal{V}$ are all such covectors except for the "bad" cotangent directions, those in the $\pm \boldsymbol{dx}_1$ codirection.

Inclusion (A.8) and Example A.5 demonstrate that $\mathcal{L}$ can give additional singularities in the set $\mathcal{A}$ (in the $\pm \boldsymbol{dx}_1$ codirection). Therefore they do not affect singularities in the visible directions, namely those in $\mathcal{V}$. In Remark A.4, we prove that these added singularities are really a smearing of singularities of f in planes conormal the bad codirections, that is, planes $x_1 = a$.

Proof. In the proof of Theorem A.2 we will follow the conventions in [13, Chapter 8] and allow wavefront directions to be in $\mathbb{R}^n \setminus 0$ rather than in the cotangent space. Let us now give an outline of the proof. If $\mathcal{L}$ were a standard PDO, then the proof would follow from standard results. Our case is complicated by the fact that $\mathcal{L}$ is not a standard PDO since its symbol,

$$\sigma(\boldsymbol{x}, \boldsymbol{\xi}) = \left(\frac{\varphi\big(\arg(\boldsymbol{\xi}') + \pi/2\big)}{\|\boldsymbol{\xi}'\|} \right) (\mu + \|\boldsymbol{\xi}'\|^2),$$

does not satisfy the decay conditions on the derivatives in the ξ_1 direction. We introduce an operator $\mathcal{M}$ (A.10) that cuts off in the ξ_1 direction and show that $\mathcal{M}$ and $\mathcal{L}$ can be composed to become a standard PDO that detects singularities of f essentially in $\mathcal{V}$. Next, we show that $(1 - \mathcal{M})\mathcal{L}$ contributes to the wavefront set only near the ξ_1 direction. Finally, we put this together to show that the wavefront in directions in $\mathcal{V}$ are visible and that the only added directions are in $\mathcal{A}$. Theorem 8.2.9 and other results in [13, section 8.2] can be used to prove parts of this theorem without introducing the operator $\mathcal{M}$. We include that operator in order to provide an elementary proof of the other properties of $\mathcal{L}$. We begin with a useful lemma.

LEMMA A.3. *Let $f \in \mathscr{S}'(\mathbb{R}^n)$, and let $U \subset \mathbb{R}^n$ be a nonempty open cone containing the vector $\boldsymbol{\xi}_0$. Assume the Fourier transform $\mathcal{F}(f)$ is zero on U except for a compact set (which could be empty). Then, for all $\boldsymbol{x}_0 \in \mathbb{R}^n$, $(\boldsymbol{x}_0, \boldsymbol{\xi}_0) \notin \mathrm{WF}(f)$, where $\mathrm{WF}(f)$ denotes the $\mathscr{C}^\infty$ wavefront set of f.*

The proof follows from [13]. In particular, $\boldsymbol{\xi}_0$ is not in the limit cone at infinity of $\mathrm{supp}\,\mathcal{F}f$, and so, by [13, Lemma 8.1.7, p. 258], for any point $\boldsymbol{x}_0$, $(\boldsymbol{x}_0, \boldsymbol{\xi}_0) \notin \mathrm{WF}(f)$.

We now define the operator $\mathcal{M}$ such that $\mathcal{M}\mathcal{L}$ is a standard PDO that detects most singularities in $\mathcal{V}$. Denote the set of second coordinates in $\mathcal{V}$ by

(A.9) $\mathcal{W} := \left\{ \boldsymbol{\xi} \in \mathbb{R}^3 \setminus 0 \mid \xi_2 \neq 0, |\xi_3/\xi_2| < \tan\theta_{\text{cut}} \right\}.$

Let U be a small conic open neighborhood of $\pm e_1$, and let U' be a conic open subset of U such that $\pm e_1 \in U'$ and $\mathrm{cl}(U') \subset (U \cup \{0\})$. Now let $m(\boldsymbol{\xi})$ be a function that is homogeneous of degree zero in $\mathbb{R}^3$, smooth away from the origin, zero in U', and equal to one off of U. Define

$$(A.10) \qquad \mathcal{M}(f)(\boldsymbol{x}) = \mathcal{F}^{-1}\big(m(\cdot)\mathcal{F}(f)(\cdot)\big)(\boldsymbol{x}).$$

Then, $\mathcal{M}$ is a classical PDO of order zero in Sobolev scale.

It is a straightforward justification using Fourier transforms that one can compose $\mathcal{L}$ with $\mathcal{M}$ (or $(1-\mathcal{M})$) for distributions of compact support, and we will assume this. $\mathcal{ML}$ is a classical PDO because its symbol,

$$m(\boldsymbol{\xi})\left(\frac{\varphi\big(\arg(\boldsymbol{\xi}') + \pi/2\big)}{\|\boldsymbol{\xi}'\|}\right)\big(\mu + \|\boldsymbol{\xi}'\|^2\big),$$

is the sum of a term homogeneous of degree (-1) and one homogeneous of degree 1. Since the terms are smooth away from the origin ($m(\xi)$ cuts off the near the nonsmooth ξ_1 direction), $\mathcal{ML}$ is a classical PDO of order one. Since its symbol is elliptic on the open set $\mathbb{R}^3 \times (\mathcal{W} \setminus \mathrm{cl}(U'))$, $\mathcal{L}$ is elliptic on that set. Furthermore, by local Sobolev continuity, the $\mathscr{H}^{\alpha+1}$ wavefront of f in $\mathbb{R}^3 \times (\mathcal{W} \setminus \mathrm{cl}(U))$ corresponds to the $\mathscr{H}^\alpha$ wavefront of $\mathcal{ML}(f)$ on that set,

$$(A.11) \quad \mathrm{WF}^\alpha\big(\mathcal{ML}(f)\big) \cap \Big(\mathbb{R}^3 \times \big(\mathcal{W} \setminus \mathrm{cl}(U)\big)\Big) = \mathrm{WF}^{\alpha+1}(f) \cap \Big(\mathbb{R}^3 \times \big(\mathcal{W} \setminus \mathrm{cl}(U)\big)\Big).$$

Because $\mathrm{supp}\big(1 - m(\boldsymbol{\xi})\big) \subset \mathrm{cl}(U)$, $\mathcal{F}\big((1 - \mathcal{M})\mathcal{L}(f)\big)$ has support contained in $\mathrm{cl}(U)$. So, by Lemma A.3,

$$(A.12) \qquad \mathrm{WF}\big((1 - \mathcal{M})\mathcal{L}(f)\big) \subset \mathbb{R}^3 \times \mathrm{cl}(U).$$

In addition, since $\mathcal{L} = \mathcal{ML} + (1 - \mathcal{M})\mathcal{L}$, the $\mathscr{H}^{\alpha+1}$ wavefront set of $\mathcal{L}(f)$ off of $\mathbb{R}^3 \times \mathrm{cl}(U)$ is the same as that of $\mathcal{ML}(f)$. Using (A.11), we see that

$$\mathrm{WF}^\alpha\big(\mathcal{L}(f)\big) \cap \Big(\mathbb{R}^3 \times \big(\mathcal{W} \setminus \mathrm{cl}(U)\big)\Big) = \mathrm{WF}^{\alpha+1}(f) \cap \Big(\mathbb{R}^3 \times \big(\mathcal{W} \setminus \mathrm{cl}(U)\big)\Big).$$

By making U arbitrarily close to e_1, we establish (A.7).

To prove the containment (A.8), we fix U, U', and $\mathcal{M}$ as above. We will now prove

$$(A.13) \quad \mathrm{WF}^\alpha\big(\mathcal{ML}(f)\big) \subset \left(\mathrm{WF}^{\alpha+1}(f) \cap \Big(\mathbb{R}^3 \times \big(\mathrm{cl}(\mathcal{W}) \setminus \mathrm{cl}(U)\big)\Big)\right) \cup \big(\mathbb{R}^3 \times \mathrm{cl}(U)\big).$$

First, because the symbol of $\mathcal{ML}$ is supported on the closed set $\mathbb{R}^3 \times \big(\mathrm{cl}(\mathcal{W}) \setminus U'\big)$,

$$\mathrm{WF}^\alpha\big(\mathcal{ML}(f)\big) \subset \mathbb{R}^3 \times \big(\mathrm{cl}(\mathcal{W}) \setminus U'\big).$$

Because of (A.11), we need only consider $\boldsymbol{\xi} \in \mathrm{bd}(\mathcal{W}) \setminus \mathrm{cl}(U)$ and $\boldsymbol{x}_0 \in \mathbb{R}^3$ such that $(\boldsymbol{x}_0, \boldsymbol{\xi}) \notin \mathrm{WF}^{\alpha+1}(f)$. Since $\mathcal{ML}$ is a standard PDO of order one, $(\boldsymbol{x}_0, \boldsymbol{\xi}) \notin \mathrm{WF}^\alpha\big(\mathcal{ML}(f)\big)$. This shows (A.13).

Next, the wavefront set of a sum is contained in the union of the wavefront set of the terms. Combining this fact with (A.12) and (A.13) yields

$$\mathrm{WF}\big(\mathcal{L}(f)\big) \subset \left(\mathrm{WF}^{\alpha+1}(f) \cap \Big(\mathbb{R}^3 \times \big(\mathrm{cl}(\mathcal{W}) \setminus \mathrm{cl}(U)\big)\Big)\right) \cup \big(\mathbb{R}^3 \times \mathrm{cl}(U)\big).$$

The inclusion in (A.8) now follows when we let U shrink to $\pm e_1$.

We claim that if f is supported in B, then $\operatorname{supp} \mathcal{L}(f) \subset [-1, 1] \times \mathbb{R}^2$. This is true by a global version of the argument at the end of Remark A.4. This concludes the proof of Theorem A.2. ☐

REMARK A.4. *Note that if $f \in \mathscr{E}'(\mathbb{R}^3)$ is smooth in the $\pm dx_1$ codirection at all points, then, for sufficiently small U, $(1 - \mathcal{M})(f)$ is smooth, and so*

$$\mathcal{L}(f) = \mathcal{M}\mathcal{L}(f) + \mathcal{L}(1 - \mathcal{M})(f)$$

has no wavefront in the $\pm d\boldsymbol{\xi}_1$ codirection. In other words, for this f there are no added singularities.

A local version of this statement is true: if $a \in \mathbb{R}$ and f is smooth in the $\pm dx_1$ codirection at all points in the plane $x_1 = a$, i.e., $\big((a, \boldsymbol{x}'); \pm dx_1\big) \notin \mathrm{WF}(f)$ for all $\boldsymbol{x}' \in \mathbb{R}^2$), then $\mathcal{L}(f)$ is smooth in the $\pm dx_1$ codirection above all points on the plane $x_1 = a$. To see this we observe that because $\operatorname{supp} f$ is compact and wavefront sets are conical and closed, one can find a function $g \in \mathscr{C}_c^\infty(\mathbb{R})$ is not zero near $x_1 = a$ and a sufficiently small neighborhood U of e_1 such that $g(x_1)(1 - \mathcal{M})(f)$ is smooth, and so $g\mathcal{L}(f)$ is smooth in the $\pm dx_1$ codirection at all points. Thus, $\mathcal{L}(f)$ is smooth in this direction at all points in the plane $x_1 = a$.

That is, wavefront is not added if f is smooth in this codirection at all points on the plane $x_1 = a$. However, Example A.5 demonstrates that wavefront can be spread in the plane $x_1 = a$ if f has wavefront in the $\pm dx_1$ direction at points in this plane.

We now introduce a new operator, $\mathcal{L}_\triangle$, which is related to an operator of Louis and Maaß for cone beam CT. Louis and Maaß adapted Lambda tomography to cone beam tomography in a very clever way [17] by taking a Laplacian in the detector plane before taking cone-beam backprojection. This adds extra singularities to the reconstruction as proven in general in [8] and for the cone beam transform in $\mathbb{R}^3$ in [7, 14]. The natural generalization of the Louis–Maaß operator to our setting is

$$(\text{A.14}) \qquad \mathcal{L}_\triangle(f) := \mathcal{P}^*_{\theta_{\mathrm{cut}}}\big((\mu - \Delta_{\boldsymbol{\omega}^\perp})\mathcal{P}(f)\big),$$

where $\Delta_{\boldsymbol{\omega}^\perp}$ is the Laplacian operator in the detector plane and $\mu \geq 0$. In Example A.5 we will show that $\mathcal{L}_\triangle$ adds stronger singularities than $\mathcal{L}$.

Anastasio et al. [1], Katsevich [15], and Ye, Yu, and Wang [31] have developed refinements of Louis and Maaß's operator for cone beam CT. They decrease the added singularities by taking a derivative in only one direction rather than taking the Laplacian in the detector plane. This is analogous to our operator $\mathcal{L}$, in which the derivative is D_σ^2. Although these results are related, they do not apply to parallel beam data, as our methods do.

The arguments in our proof of Theorem A.1 can be used to show that $\mathcal{L}_\triangle$ is a PDO with a singular symbol

$$\left(\frac{\varphi(\arg(\boldsymbol{\xi}') + \pi/2)}{\|\boldsymbol{\xi}'\|}\right)\big(\mu + \|\boldsymbol{\xi}\|^2\big)$$

and (A.7) and (A.8) hold for $\mathcal{L}_\triangle$. For fixed $\boldsymbol{\xi}'$, the symbol of $\mathcal{L}_\triangle$ is of order 2 as $\boldsymbol{\xi}_1 \to \infty$, although it is of order 1 in other directions. The symbol of $\mathcal{L}$ is more mildly singular since, although it is not differentiable when $\boldsymbol{\xi}' = \mathbf{0}$ (on the ξ_1-axis), it is of order zero as $\boldsymbol{\xi}_1 \to \infty$ when $\boldsymbol{\xi}'$ is fixed.

Our next example justifies the addition of the set $\mathcal{A}$ in (A.8), a set on which wavefront can be added by $\mathcal{L}$ and $\mathcal{L}_\triangle$. The example also shows how $\mathcal{L}_\triangle$ adds stronger singularities than $\mathcal{L}$.

EXAMPLE A.5. *Let $\alpha \in \mathbb{R}$, and let $\epsilon > 0$ be arbitrary. We construct a function $f \in \mathscr{H}^{\alpha+1}(\mathbb{R}^3)$ supported in $S := [-1/2, 1/2]^3$ with the following properties:*

1. *$\mathcal{L}_\triangle(f) \notin \mathscr{H}^{\alpha}_{\mathrm{loc}}(\mathbb{R}^3)$, and $\mathcal{L}_\triangle(f)$ has $\mathscr{H}^{\alpha}$ wavefront set in the $\pm d\boldsymbol{x}_1$ direction even though f is in $\mathscr{H}^{\alpha+1}$ everywhere. This is true even for points outside $\mathrm{supp}\, f$, points at which f is smooth.*
2. *$\mathcal{L}(f)$ is in $\mathscr{H}^{\alpha+1}_{\mathrm{loc}}(\mathbb{R}^3)$ but has $\mathscr{H}^{\alpha+1+\epsilon}$ wavefront set in the $\pm d\boldsymbol{x}_1$ codirection outside of $\mathrm{supp}\, f$. Therefore, $\mathcal{L}$ also spreads singularities, but, for this case, the singularities are weaker. This weakening is suggested by the fact that $\mathcal{L}^0$, which is defined as $\mathcal{L}$ with $\mu = 0$, is continuous of order one in Sobolev scale.*

The actual construction of f goes as follows: Let $\epsilon' = \min\{\epsilon, 1/2\}$, and let $\phi_1 \in \mathscr{H}^{\alpha+1}(\mathbb{R})$ with $\mathrm{supp}\, \phi_1 = [-1/2, 1/2]$ such that

(A.15) $$\mathrm{WF}^{\alpha+1+\epsilon'}(\phi_1) = \big\{(x_1, t d\boldsymbol{x}_1) \mid x_1 \in [-1/2, 1/2],\, t \neq 0\big\}.$$

Also, let ϕ_2 be a nonnegative smooth function in $\mathbb{R}^2$ with $\mathrm{supp}\, \phi_2 = [-1/2, 1/2]^2$.

For $x_1 \in \mathbb{R}$ and $\boldsymbol{x}' \in \mathbb{R}^2$ define $f(x_1, \boldsymbol{x}') = \phi_1(x_1)\phi_2(\boldsymbol{x}')$. For $g \in \mathscr{C}_c^\infty(\mathbb{R}^2)$ define

(A.16) $$\mathcal{H}(g)(\boldsymbol{x}') := \int_{\boldsymbol{y}' \in \mathbb{R}^2} \frac{\varphi\big(\arg(\boldsymbol{y}')\big)}{\|\boldsymbol{y}'\|} g(\boldsymbol{x}' + \boldsymbol{y}')\, d\boldsymbol{y}';$$

then $\mathcal{H}$ is really $\mathcal{P}^*_{\theta_{\mathrm{cut}}}\mathcal{P}$ restricted to a fixed plane (compare with (A.2)). Since $\mathcal{H}$ is a classical PDO, $\mathcal{H}$ is continuous from domain $\mathscr{C}_c^\infty(S)$ to $\mathscr{C}^\infty(\mathbb{R}^2)$.

It is straightforward to show that $\mathcal{L}_\triangle(f) = -\phi_1'' \mathcal{H}(\phi_2) + \phi_1 \mathcal{H}\big((\mu - \Delta_{\boldsymbol{x}'})\phi_2\big)$, where ϕ_1'' is the second derivative of ϕ_1. Since ϕ_1 is chosen to be in $\mathscr{H}^{\alpha+1}$ and not $\mathscr{H}^{\alpha+1+\epsilon'}$, the first term in the expression for $\mathcal{L}_\triangle(f)$ is not in $\mathscr{H}^{\alpha}_{\mathrm{loc}}$, although the other terms are. Thus, $\mathcal{L}_\triangle(f)$ is not in $\mathscr{H}^{\alpha}_{\mathrm{loc}}$. Because of (A.15),

(A.17) $$\mathrm{WF}^{\alpha}\big(\mathcal{L}_\triangle(f)\big) = \big\{(x_1, \boldsymbol{x}', t d\boldsymbol{x}_1) \mid x_1 \in [-1/2, 1/2],\, \boldsymbol{x}' \in \mathrm{supp}\, \mathcal{H}(\phi_2),\, t \neq 0\big\}.$$

Furthermore, since φ_2 is nonnegative and not the zero function, $\mathcal{H}(\varphi_2)$ has unbounded support. Thus $\mathcal{L}_\triangle$ adds Sobolev wavefront both inside and outside $\mathrm{supp}\, f$ even though $f \in \mathscr{H}^{\alpha+1}_c(\mathbb{R}^3)$.

In a similar way, one shows that $\mathcal{L}(f) = \phi_1 \mathcal{H}\big((\mu - \Delta_{\boldsymbol{x}'})\phi_2\big)$, and so $\mathcal{L}f$ is in $\mathscr{H}^{\alpha+1}_{\mathrm{loc}}$ (because ϕ_1 is in $\mathscr{H}^{\alpha+1}$ and the other term is smooth), but

$$\mathrm{WF}^{\alpha+1+\epsilon'}\big(\mathcal{L}(f)\big)$$
$$= \Big\{(x_1, \boldsymbol{x}', t d\boldsymbol{x}_1) \mid x_1 \in [-1/2, 1/2],\, \boldsymbol{x}' \in \mathrm{supp}\, \mathcal{H}\big((\mu - \Delta_{\boldsymbol{x}'})\phi_2\big),\, t \neq 0\Big\}.$$

Note that $\mathrm{supp}\, \mathcal{H}\big((\mu - \Delta_{\boldsymbol{x}'})\phi_2\big)$ must be unbounded,[10] so $\mathcal{L}$ spreads singularities of f, but they are weaker than those for $\mathcal{L}_\triangle(f)$.

To state Theorem 6.3, we need a little more notation. Covectors in $T^*(Y)$ will be denoted by $\big((y_1, y_{\boldsymbol{\sigma}}, \theta);\, \nu_1 d\boldsymbol{y}_1 + \nu_{\boldsymbol{\sigma}} d\boldsymbol{y}_{\boldsymbol{\sigma}} + \nu_3 d\boldsymbol{\theta}\big)$, where $(\nu_1, \nu_{\boldsymbol{\sigma}}, \nu_\theta) \in \mathbb{R}^3$ and $d\boldsymbol{y}_1$ is the covector dual to the tangent vector $\partial/\partial y_1$, $d\boldsymbol{y}_{\boldsymbol{\sigma}}$ is dual to $\partial/\partial y_\sigma$, and $d\boldsymbol{\theta}$ is dual to $\partial/\partial\theta$. Using these conventions we can state the following theorem that gives the basic microlocal analysis of $\mathcal{P}$ with the limited data given in our ET problem.

THEOREM A.6. *Let f be a distribution of compact support on $\mathbb{R}^3$, $\theta_{\max} \in\,]0, \pi/2[$, and assume $\mathcal{P}(f)(\boldsymbol{y}, \theta)$ is given on an open set $U \subset Y$. Moreover, let $(y_1, y_{\boldsymbol{\sigma}}, \theta_0) \in U$,*

---

[10]The two-dimensional version of the proof of (A.3) shows that the two-dimensional Fourier transform $\mathcal{F}\mathcal{H}(\phi_2)$ is a product including $\varphi(\arg(\boldsymbol{\xi}') + \pi/2)$ and so is zero on an open set. If $\mathcal{H}(\phi_2)$ had compact support, then $\phi_2 = 0$ since $\mathcal{F}\mathcal{H}(\phi_2)$ would be real-analytic.

let $\boldsymbol{\xi}_0$ be a nonzero vector perpendicular to $\boldsymbol{\omega}(\theta_0)$ written as $\boldsymbol{\xi}_0 = \xi_1 \boldsymbol{e}_1 + \xi_{\boldsymbol{\sigma}} \boldsymbol{\sigma}(\theta_0)$, and assume $\xi_{\boldsymbol{\sigma}} \neq 0$ (i.e., $\boldsymbol{\xi}_0$ is not parallel to $\boldsymbol{e}_1$). Finally, let $\boldsymbol{x}_0 \in \ell(y_1, y_{\boldsymbol{\sigma}}, \theta_0)$. Then, $(\boldsymbol{x}_0; \boldsymbol{\xi}_0 \boldsymbol{dx}) \in \mathrm{WF}^{\alpha}(f)$ if and only if

$$(A.18) \qquad \Big((y_1, y_{\boldsymbol{\sigma}}, \theta_0); \xi_1 \boldsymbol{dy}_1 + \xi_{\boldsymbol{\sigma}} \boldsymbol{dy}_a + \big(\xi_{\boldsymbol{\sigma}} \boldsymbol{x} \cdot \boldsymbol{\omega}(\theta_0)\big) \boldsymbol{d\theta} \Big) \in \mathrm{WF}^{\alpha+1/2}\big(\mathcal{P}(f)\big).$$

The proof follows from the fundamental results in [9] that show that Radon transforms are FIOs and also from the analysis of the general X-ray transform in [8] (see also [2]). The proof involves first calculating the canonical relation of $\mathcal{P}$, next noting that $\mathcal{P}$ is elliptic, and finally using the calculus of FIOs [12] to tell what $\mathcal{P}f$ does to the wavefront set. A proof of this result is given for more general curves of directions in S^2 given in [22].

REFERENCES

[1] M. A. ANASTASIO, Y. ZOU, E. Y. SIDKY, AND X. PAN, *Local cone-beam tomography image reconstruction on chords*, J. Opt. Soc. Amer. A, 24 (2007), pp. 1569–1579.

[2] J. BOMAN AND E. T. QUINTO, *Support theorems for real analytic Radon transforms on line complexes in $\mathbb{R}^3$*, Trans. Amer. Math. Soc., 335 (1993), pp. 877–890.

[3] D. J. DE ROSIER AND A. KLUG, *Reconstruction of three dimensional structures from electron micrographs*, Nature, 217 (1968), pp. 130–134.

[4] D. FANELLI AND O. ÖKTEM, *Electron tomography: A short overview with an emphasis on the absorption potential model for the forward problem*, Inverse Problems, 24 (2008), 013001.

[5] A. FARIDANI, D. V. FINCH, E. L. RITMAN, AND K. T. SMITH, *Local tomography* II, SIAM J. Appl. Math., 57 (1997), pp. 1095–1127.

[6] A. FARIDANI, E. L. RITMAN, AND K. T. SMITH, *Local tomography*, SIAM J. Appl. Math., 52 (1992), pp. 459–484.

[7] D. V. FINCH, I.-R. LAN, AND G. UHLMANN, *Microlocal analysis of the restricted X-ray transform with sources on a curve*, in Inside Out: Inverse Problems and Applications, Math. Sci. Res. Inst. Publ. 47, G. Uhlmann, ed., Cambridge University Press, Cambridge, UK, 2003, pp. 193–218.

[8] A. GREENLEAF AND G. UHLMANN, *Non-local inversion formulas for the X-ray transform*, Duke Math. J., 58 (1989), pp. 205–240.

[9] V. GUILLEMIN AND S. STERNBERG, *Geometric Asymptotics*, AMS, Providence, RI, 1977.

[10] P. W. HAWKES AND E. KASPER, *Principles of Electron Optics. Volume 3. Wave Optics*, Academic Press, London, 1994.

[11] W. HOPPE, R. LANGER, G. KNESCH, AND C. POPPE, *Protein-kristallstrukturanalyse mit elektronenstrahlen*, Naturwissenschaften, 55 (1968), pp. 333–336.

[12] L. HÖRMANDER, *Fourier integral operators,* I, Acta Math., 127 (1971), pp. 79–183.

[13] L. HÖRMANDER, *The Analysis of Linear Partial Differential Operators*, Vol. I, Springer-Verlag, New York, 1983.

[14] A. I. KATSEVICH, *Cone beam local tomography*, SIAM J. Appl. Math., 59 (1999), pp. 2224–2246.

[15] A. I. KATSEVICH, *Improved cone beam local tomography*, Inverse Problems, 22 (2006), pp. 627–643.

[16] P. KUCHMENT, K. LANCASTER, AND L. MOGILEVSKAYA, *On local tomography*, Inverse Problems, 11 (1995), pp. 571–589.

[17] A. K. Louis and P. Maaß, *Contour reconstruction in 3-D X-ray CT*, IEEE Trans. Med. Imaging, 12 (1993), pp. 764–769.

[18] F. Natterer and F. Wübbeling, *Mathematical Methods in Image Reconstruction*, SIAM Monogr. Math. Model. Comput. 5, SIAM, Philadelphia, 2001.

[19] B. Petersen, *Introduction to the Fourier Transform and Pseudo-Differential Operators*, Pitman, Boston, 1983.

[20] E. T. Quinto, *Singularities of the X-ray transform and limited data tomography in $\mathbb{R}^2$ and $\mathbb{R}^3$*, SIAM J. Math. Anal., 24 (1993), pp. 1215–1225.

[21] E. T. Quinto, *Local algorithms in exterior tomography*, J. Comput. Appl. Math., 199 (2007), pp. 141–148.

[22] E. T. Quinto, T. Bakhos, and S. Chung, *Local tomography in 3-D SPECT*, in Proceedings of the Interdisciplinary Workshop on Mathematical Methods in Biomedical Imaging and Intensity-Modulated Radiation Therapy (IMRT), Pisa, Italy, 2007, to appear.

[23] L. Reimer, *Transmission Electron Microscopy*, 4th ed., Springer Ser. Opt. Sci. 36, Springer-Verlag, New York, 1997.

[24] S. Sandin, L.-G. Öfverstedt, A. C. Wikström, O. Wrange, and U. Skoglund, *Structure and flexibility of individual immunoglobulin G molecules in solution*, Structure, 12 (2004), pp. 409–415.

[25] V. I. Semyanistyi, *Homogeneous functions and some problems of integral geometry on spaces of constant curvature*, Soviet Math. Dokl., 2 (1961), pp. 59–62.

[26] K. T. Smith, *Inversion of the X-ray transform*, in Inverse Problems, SIAM-AMS Proc. 14, AMS, Providence, RI, 1984, pp. 41–52.

[27] K. Tryggvason, J. Patrakka, and J. Wartiovaara, *Hereditary proteinuria syndromes and mechanisms of proteinuria*, New England J. Medicine, 354 (2006), pp. 1387–1401.

[28] E. I. Vainberg, I. A. Kazak, and V. P. Kurozaev, *Reconstruction of the internal three-dimensional structure of objects based on real-time integral projections*, Soviet J. Nondestructive Testing, 17 (1981), pp. 415–423.

[29] B. K. Vainshtein, V. V. Barynin, and G. V. Gurskaya, *The hexagonal crystalline structure of catalase and its molecular structure*, Dokl. Akad. Nauk SSSR, 182 (1968), pp. 569–572 (in Russian); Soviet Phys. Dokl., 13 (1969), pp. 838–841 (in English).

[30] J. Wartiovaara, L.-G. Öfverstedt, J. Khoshnoodi, J. Zhang, E. Makela, S. Sandin, V. Ruotsalainen, R. H. Cheng, H. Jalanko, U. Skoglund, and K. Tryggvason, *Nephrin strands contribute to a porous slit diaphragm scaffold as revealed by electron tomography*, J. Clin. Invest., 114 (2004), pp. 1475–1483.

[31] Y. Ye, H. Yu, and G. Wang, *Cone beam pseudo-lambda tomography*, Inverse Problems, 23 (2007), pp. 203–215.

[32] J. M. Zuo, *Electron detection characteristics of a slow-scan CCD camera, imaging plates and film, and electron image restoration*, Microsc. Res. Tech., 49 (2000), pp. 245–268.